DOI: 10.1002/anie.201307976

Lithium–Air Batteries

Core–Shell-Structured CNT@RuO$_2$ Composite as a High-Performance Cathode Catalyst for Rechargeable Li–O$_2$ Batteries**

*Zelang Jian, Pan Liu, Fujun Li, Ping He, Xianwei Guo, Mingwei Chen, and Haoshen Zhou**

Abstract: *A RuO$_2$ shell was uniformly coated on the surface of core CNTs by a simple sol–gel method, and the resulting composite was used as a catalyst in a rechargeable Li–O$_2$ battery. This core–shell structure can effectively prevent direct contact between the CNT and the discharge product Li$_2$O$_2$, thus avoiding or reducing the formation of Li$_2$CO$_3$, which can induce large polarization and lead to charge failure. The battery showed a high round-trip efficiency (ca. 79 %), with discharge and charge overpotentials of 0.21 and 0.51 V, respectively, at a current of 100 mA g$_{total}^{-1}$. The battery also exhibited excellent rate and cycling performance.*

Rechargeable lithium–oxygen (Li–O$_2$) batteries were first introduced by Abraham and Jiang in 1996.[1] These batteries have a very large theoretical gravimetric energy (3505 Wh kg^{-1} based on the reversible reaction of $2\,Li + O_2 \rightarrow Li_2O_2$) and have been attracting increasing attention in recent years.[2] Li–O$_2$ batteries can deliver five times the energy density observed for Li-ion batteries and are thus promising for electric-vehicle applications.[3] However, the development of rechargeable Li–O$_2$ batteries faces a lot of challenges, such as low round-trip efficiency, low rate capability, a poor cycle life, and electrolyte instability.[4]

A typical rechargeable Li–O$_2$ battery is composed of a lithium-metal anode, an organic electrolyte, and a porous cathode exposed to O$_2$ during cell operation. On discharge, O$_2$ is reduced when it enters the porous cathode and combines with Li$^+$ to form solid Li$_2$O$_2$, which is decomposed during the charging process. Until now, carbon has been widely used as a cathode catalyst in rechargeable Li–O$_2$ batteries.[5] Its overpotential is as large as 1.5 V, which induces a low round-trip efficiency (53–64 %[6]). Carbon has a discharge overpotential of approximately 0.3 V and a charge overpotential higher than 1 V; these values indicate that carbon exhibits sufficient catalytic activity for the oxygen-reduction reaction (ORR) but low catalytic activity for the oxygen-evolution reaction (OER).[5,6] The OER catalytic activity for carbon-based catalysts is more crucial. Metal or metal-oxide nanoparticles have been added to reduce the charge overpotential.[7] In this way, the corresponding round-trip efficiency can be enhanced.

McCloskey et al.[3a] recently found that a carbon electrode can react with Li$_2$O$_2$ to form Li$_2$CO$_3$. Gallant et al.[8] confirmed the reaction between the carbon electrode and Li$_2$O$_2$. To avoid this reaction, carbon-free electrodes were suggested.[9] Peng et al.[10] introduced porous Au as a catalyst in rechargeable Li–O$_2$ batteries. They reported reversible formation/decomposition of the main discharge product Li$_2$O$_2$ and excellent cycling performance. However, the use of carbon-free electrodes, such as metals and metal oxides, has some disadvantages. Noble metals are expensive, and other metals can be oxidized easily or have little catalytic activity. Most metal oxides suffer from low electronic conductivity. Furthermore, the synthesis of porous electrodes with a high surface area is not an easy task. Although carbon and metal (oxide) composites are good catalysts in rechargeable Li–O$_2$ batteries, the exposed carbon will react with Li$_2$O$_2$ to form Li$_2$CO$_3$, which results in bad electrochemical performance. Special structured materials are expected to prevent or decrease the formation of Li$_2$CO$_3$. Materials with a metal (oxide) shell and a carbon core are expected to offer many advantages, such as: 1) the avoidance of direct contact between carbon and the discharge product Li$_2$O$_2$ to prevent their reaction, 2) a combination of the good OER catalytic activity of metals or metal oxides and the high conductivity of carbon, and 3) preservation of the initial structure with a high specific surface area.

Ru- and RuO$_2$-based materials used as cathodes in Li–O$_2$ batteries have exhibited good catalytic activity towards both the ORR and the OER.[11] Herein, we report a simple sol–gel method for the synthesis of a RuO$_2$–carbon-nanotube (CNT@RuO$_2$) composite, which features a CNT core with a diameter of about 15 nm and an RuO$_2$ shell with a thickness of about 3.5 nm. The electrochemical performance of a Li–O$_2$ battery with the CNT@RuO$_2$ composite as the cathode was investigated in detail.

The CNT@RuO$_2$ composite was prepared by a sol–gel method.[12] Acid-treated carbon nanotubes were dispersed in a solution of RuCl$_3$ by ultrasonication, and an aqueous

---

[*] Dr. Z. L. Jian, Dr. F. J. Li, Prof. H. S. Zhou
Energy Technology Research Institute, National Institute of Advanced Industrial Science and Technology (AIST)
Umezono 1-1-1, Tsukuba, 305-8568 (Japan)
E-mail: hs.zhou@aist.go.jp

Dr. P. Liu, Dr. X. W. Guo, Prof. M. W. Chen
WPI Advanced Institute for Materials Research, Tohoku University
Sendai, 980-8577 (Japan)
and
CREST, JST
4-1-8 Honcho Kawaguchi, Saitama, 332-0012 (Japan)

Dr. P. He, Prof. H. S. Zhou
National Laboratory of Solid State Microstructures and Department of Energy Science and Engineering, Nanjing University
Nanjing, 210093 (China)

[**] This research was partially supported financially by the Japanese Funding Program for World-Leading Innovative R&D on Science and Technology (FIRST Program) and Chinese Fund (2014CB932300).

Supporting information for this article is available on the WWW under http://dx.doi.org/10.1002/anie.201307976.

solution of $NaHCO_3$ was slowly added to adjust the pH value to 7. The as-obtained precipitate was then washed several times and dried at 50 °C. After annealing, the final product was denoted as CNT@RuO_2 (see Figure S1 in the Supporting Information for X-ray diffraction (XRD) patterns of the CNT and CNT@RuO_2 samples). Two diffraction peaks at 25.9 and 42.8° can be assigned to the (002) and (100) planes of the CNTs, respectively; these features indicate good crystallinity. When RuO_2 was coated on the CNTs (CNT@RuO_2), the diffraction peaks of the CNTs were still visible but sharply decreased. Moreover, two broad humps, ascribed to RuO_2, appeared at around 32 and 54°. On the basis of the N_2-sorption measurement, the specific surface area of the pristine-CNT and CNT@RuO_2 samples was 186 and 72.7 $m^2 g^{-1}$, respectively (see Figure 1 a). The lower surface area of CNT@RuO_2 can be attributed to the dense RuO_2 coating. The CNT content in the CNT@RuO_2 composite was evaluated by thermogravimetric (TG) analysis to be 26 % in an O_2 flow (see Figure S2 for the TG curve). However, the specific surface area of the CNT@RuO_2 composite was still high, thus suggesting that a porous structure remained.

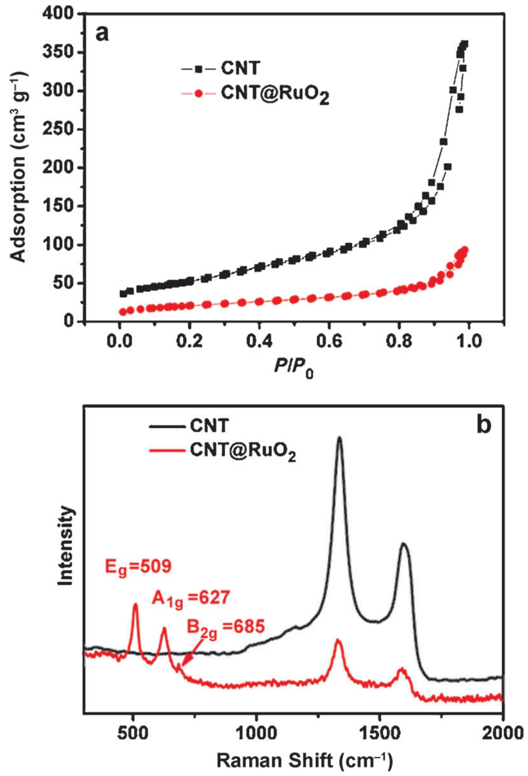

Figure 1. a) Nitrogen-adsorption–desorption isotherms and b) Raman spectra of the pristine-CNT and CNT@RuO_2 samples.

To further investigate the distribution and composition of the surface coating layer, we carried out Raman spectroscopy, scanning electron microscopy (SEM), and scanning transmission electron microscopy (STEM). Figure 1 b shows the Raman spectra of the pristine-CNT and CNT@RuO_2 samples. Both samples exhibit a D-band at around 1336 cm^{-1} and a G-band at around 1597 cm^{-1}, which are characteristic bands of carbonaceous materials.[13] The band intensities in the CNT@RuO_2 sample were significantly small: they were only about 1/5 of those observed for the pristine-CNT sample. In particular, three new peaks located at 509, 627, and 685 cm^{-1} were observed in the CNT@RuO_2 sample. These peaks correspond to the three Raman active modes of RuO_2: the E_g, A_{1g}, and B_{2g} modes, respectively.[14] The intensity of the A_{1g} mode is related to the residual stress, that is, a low residual stress means a strong A_{1g} mode.[14b] Furthermore, materials with low residual stress exhibit a stable structure. Therefore, the strong A_{1g} mode in the CNT@RuO_2 sample suggests high stability. The as-received CNTs showed a one-dimensional morphology, with diameters of about ten or tens of nanometers and lengths of several micrometers (see Figures S3 and S4 for the SEM images of the pristine-CNT and CNT@RuO_2 samples, respectively). Upon coating with RuO_2, the surface became rough; however, the one-dimensional morphology was maintained well in CNT@RuO_2. These results are in agreement with the BET results with respect to the specific surface area of the samples. A bright-field (BF) STEM image (see Figure S5) confirmed the presence of a coating layer of RuO_2 around the CNTs and the retention of CNT features in CNT@RuO_2. Almost all of the RuO_2 was uniformly coated on the surface of the CNTs. The resulting diameters of the CNT@RuO_2 structures increased to about 20–30 nm.

We used energy-dispersive X-ray (EDX) mapping to further investigate the distribution and composition of the composite. EDX maps of the elements C, Ru, and O and the composite are shown in Figure 2 a. The C element is distributed as a hollow tube with a diameter of 15 nm, which is in agreement with the typical features of CNTs. The Ru and O elements are uniformly distributed around a single CNT. In the composite image in Figure 2 a, the distribution of the elements Ru, O, and C clearly indicates the presence of a uniform coating layer of RuO_2 around the CNT. The complete overlap between Ru and O suggests that the coating layer is RuO_2, not metal Ru. The diameter of the resulting composite CNT@RuO_2 had increased to about 22 nm from 15 nm in the pristine CNT. The STEM results indicate that the thickness of the RuO_2 coating layer is about 4 nm. Large-scale EDX maps of the composite CNT@RuO_2 (see Figure S6) suggested that RuO_2 was uniformly coated on all the CNTs and distributed in the whole sample. Furthermore, the tubular structure was maintained well, thus suggesting its porous nature. Figure 2 b,c shows the dark-field (HAADF) and BF-STEM images, respectively. The core–shell configuration of the CNT@RuO_2 can be clearly observed. The corresponding schematic diagram is shown in the Figure 2 d, which clearly and vividly displays the structure of the CNT@RuO_2 sample. The enlarged HAADF-STEM image in Figure 2 e (see also Figure S7) shows the RuO_2 nanoparticles with crystal lattices in some areas. These results indicate that RuO_2 nanoparticles can be uniformly coated onto CNTs at a thickness of about 4 nm by the applied sol–gel method.

The pristine-CNT and CNT@RuO_2 samples were both used as cathode catalysts in rechargeable Li–O_2 batteries. The O_2 cathodes were prepared by coating a paste of the CNT or CNT@RuO_2 sample (90 wt %) and polytetrafluoroethylene

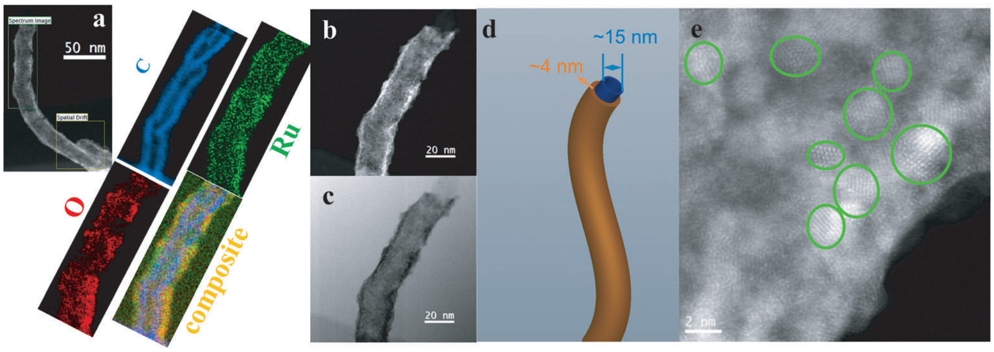

Figure 2. a) HAADF-STEM image and EDX maps (of the C, Ru, and O elements and of all three elements in the composite) of the CNT@RuO_2 sample. The green box highlights the spectrum image, the yellow box highlights the spatial drift. b) HAADF-STEM and c) BF-STEM images of a single CNT@RuO_2 structure (space bars: 20 nm). d) Schematic diagram of a single CNT@RuO_2 structure. e) Enlarged HAADF-STEM image (space bar: 2 nm).

(PTFE, 10 wt%) onto a Ti mesh. No additional conductive additives were applied. Li–O_2 batteries containing the catalytic electrode and a Li electrode in a tri(ethylene glycol) dimethyl ether–lithium bis(trifluoromethane)sulfonamide (LiTFSI-G3, 1:5) electrolyte[15] were constructed as described in the Supporting Information. The first discharge and charge curves of the Li–O_2 battery with CNT@RuO_2 are compared with those of the Li–O_2 battery with the pristine CNTs at the same rate (based on the carbon mass) in Figure 3a to enable an understanding of the effect of the RuO_2 coating layer of CNT@RuO_2 on its ORR and OER kinetics. The Li–O_2 battery with the CNT sample shows a discharge and charge overpotential of 0.32 and 1.49 V, respectively, which lead to a low round-trip efficiency close to 59%. The delivered specific capacity reached a value as high as 3258 mA h g^{-1}. In contrast, the Li–O_2 battery with CNT@RuO_2 exhibited discharge and charge overpotentials of 0.21 and 0.51 V, respectively, which resulted in a higher round-trip efficiency of about 79% and a specific capacity of about 4350 mA h g^{-1}. The discharge voltage of the battery with CNT@RuO_2 was about 0.11 V higher than that of the battery with the pristine CNTs, thus suggesting that CNT@RuO_2 has a better ORR catalytic activity than the CNTs only. Moreover, the charge average voltage of the battery with CNT@RuO_2 was about 3.47 V, which is substantially lower than that of the battery with pristine CNTs (ca. 4.45 V) by 0.98 V, which indicates the superior OER catalytic activity of CNT@RuO_2 over CNTs only. These results demonstrate that CNT@RuO_2 can be used as a good bifunctional ORR and OER catalyst in Li–O_2 batteries.

The effects of current density on the discharge/charge voltages of Li–O_2 batteries with CNT@RuO_2 were further investigated. The RuO_2 on the surface of the CNTs has a crucial function in the OER, and the CNTs provide facile electron conduction and support for the RuO_2 coating layer. The resulting CNT@RuO_2 sample can be used as a bifunctional catalyst in Li–O_2 batteries. Therefore, the performance of Li–O_2 batteries with CNT@RuO_2 was further investigated on the basis of the total mass of the CNT@RuO_2-composite cathode. As depicted in Figure 2b, the Li–O_2 battery with CNT@RuO_2 delivered a specific discharge

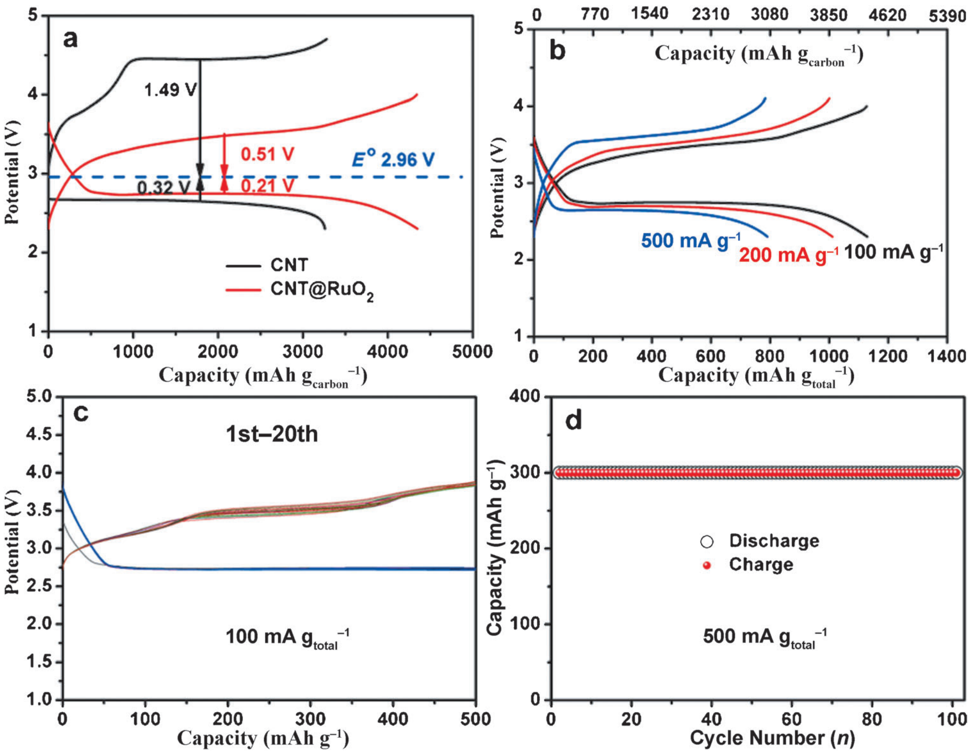

Figure 3. a) Discharge/charge profiles of the Li–O_2 batteries with the pristine CNTs (2.3–4.7 V) and CNT@RuO_2 composite (2.3–4 V) at a current of 385 mA g_{carbon}^{-1}. b) The first discharge/charge profiles of Li–O_2 batteries with CNT@RuO_2 at a current of 100, 200, and 500 mA g_{total}^{-1}. c) First 20 cycles of discharge and charge profiles of the Li–O_2 battery at a current of 100 mA g_{total}^{-1}. d) Cycling stability of the Li–O_2 battery at a current of 500 mA g_{total}^{-1}.

capacity of 1130 mA h g^{-1} (4350 mA h g^{-1} based on carbon) and a charge capacity of 1128 mA h g^{-1} (4343 mA h g^{-1} based on carbon) at a current of 100 mA $g_{total}{}^{-1}$, thereby presenting a high coulombic efficiency close to 100 %. At higher current densities, the specific capacity decreased to 1012 and 790 mA h g^{-1} at currents of 200 and 500 mA $g_{total}{}^{-1}$, respectively. The corresponding capacity retention was 90 and 70 %, respectively, whereas the coulombic efficiencies were still close to 100 %. The high rate performance can be attributed to the core–shell structure of the CNT@RuO_2 sample, which is characterized by the high electronic conductivity of the CNTs and the good catalytic activity of RuO_2 and prevents the direct contact of the CNTs with the electrolyte and discharge product to effectively avoid side reactions. The charge/discharge average voltages were 2.69/3.56 V at a current of 200 mA $g_{total}{}^{-1}$ and 2.65/3.62 V at a current of 500 mA $g_{total}{}^{-1}$. The overpotentials slightly increased by about 150 and 250 mV, respectively, as compared with those of the cell cycled at a current of 100 mA $g_{total}{}^{-1}$. However, even at a high current of 500 mA $g_{total}{}^{-1}$ (1925 mA $g_{carbon}{}^{-1}$), the discharge average voltage was similar to that of the battery with pristine CNTs, but the charge average voltage was significantly lower than that of the battery with pristine CNTs. These results further confirm that CNT@RuO_2 is an excellent bifunctional catalyst for ORR and OER in Li–O_2 batteries.

Figure 3 c shows the typical discharge and charge profiles of the Li–O_2 battery with CNT@RuO_2 over 20 cycles at a fixed capacity of 500 mA h g^{-1} (with a depth of discharge of about 40 %, that is, ca. 40 % DOD) and a current of 100 mA $g_{total}{}^{-1}$. The battery presents perfect cycling stability over 20 cycles. Almost no variation in both the discharge and charge voltages was observed. The cycling stability of the Li–O_2 battery with CNT@RuO_2 at a high current of 500 mA $g_{total}{}^{-1}$ and a cutoff capacity of 300 mA h g^{-1} (close to 40 % DOD) is shown in Figure 3 d. The specific capacity presented no decay over 100 cycles, which indicates that the Li–O_2 batteries with CNT@RuO_2 are highly stable at various currents and show sustained performance during a large number cycles.

We conducted XRD and STEM measurements to identify the discharge products of Li–O_2 batteries with CNT@RuO_2. XRD patterns of the CNT@RuO_2 electrodes at different states for the first cycle at a current of 100 mA $g_{total}{}^{-1}$ are shown in Figure 4 a. As compared with the XRD pattern of the fresh electrode, new diffraction peaks were observed for the discharged electrode. Although these peaks were very weak, they can be reasonably assigned as the (100), (101), and (110) peaks of Li_2O_2 (as highlighted in Figure 4 a). These peaks indicate that Li_2O_2 is a major crystalline discharge product. The diffraction peaks of Li_2O_2 disappeared when the battery was recharged to 4 V, which suggests that the discharge product Li_2O_2 is decomposed in the charging process. The Li_2O_2 nanoparticles formed in the discharging process were directly observed by STEM (inset of Figure 4 b). The particle size is very small (ca. 30 nm), which is in accordance with the weak XRD signals of Li_2O_2. The presence of the discharge product Li_2O_2 was further confirmed by the selected area electron diffraction (SAED) patterns of the discharged CNT@RuO_2 electrode, the characteristic diffraction spots of which are shown in Figure 4 b. The diffraction signals observed, apart from those of the CNT, correspond to the (020), (021), (220), and (025) crystalline planes of Li_2O_2. The subsequent decomposition of Li_2O_2 in the charging process was evident from the SAED pattern of the charged electrode, in which only in the diffraction spots of the CNT were observed (Figure 4 c). Furthermore, no nanoparticles were observed in the STEM image of the recharged electrode, as shown in the inset in Figure 4 c. These results indicate that Li_2O_2, as the major discharge product, is reversibly formed in a discharging process and can be decomposed in the following charging process.

FTIR spectra were collected for the initial discharged and charged CNT and CNT@RuO_2 electrodes at a current of 100 mA $g_{total}{}^{-1}$ (Figure 4 d). The IR transmission peaks at around 600 cm^{-1} are derived from Li_2O_2 in the discharged CNT and CNT@RuO_2 electrodes, and their disappearance in the charged electrode indicates the decomposition of Li_2O_2 in the following charging process. In particular, the transmission peaks at around 1550 cm^{-1} are the signature of Li_2CO_3. In the discharged CNT@RuO_2 electrode, small transmission peaks ascribed to Li_2CO_3 were detected (Figure 4 d) and may be attributed to the partial decomposition of the ether-based

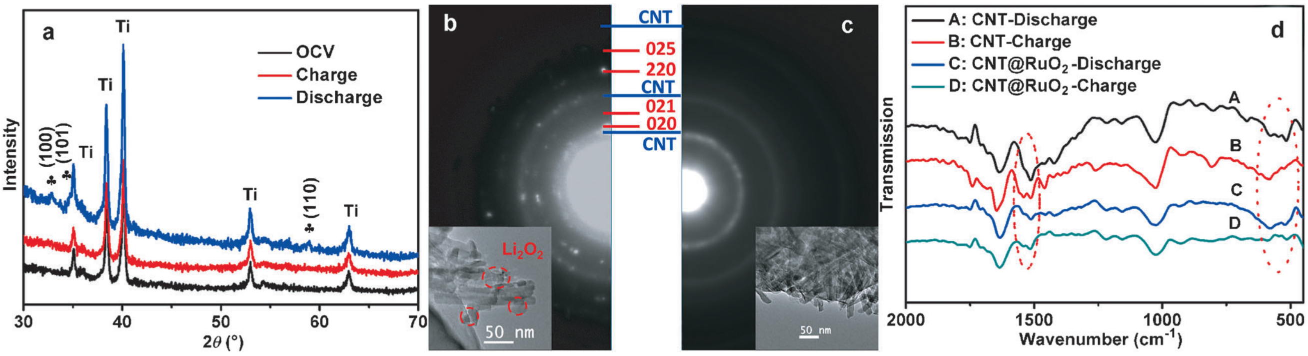

Figure 4. a) XRD patterns of the fresh, discharged, and charged CNT@RuO_2 electrodes (OCV = open-circuit voltage). b) SAED pattern of the discharged CNT@RuO_2 electrode; the inset is a TEM image of the discharged electrode. c) SAED pattern of the charged CNT@RuO_2 electrode; the inset is a TEM image of the charged electrode (space bar: 50 nm). d) FTIR spectra of the discharged/charged pristine-CNT and CNT@RuO_2 electrodes.

electrolyte.[2e] However, these peaks are significantly weaker than those of the discharged pristine-CNT electrode, maybe owing to the prevention of the side reaction between carbon and the discharge product Li_2O_2 to form Li_2CO_3 by the uniform coating of RuO_2 around the CNT. After charging, the transmission peaks of Li_2CO_3 were still observed in the spectrum of the CNT@RuO_2 electrode. However, the amount of Li_2CO_3 in the pristine-CNT electrode appeared to decrease, because the decomposition potential of Li_2CO_3 is higher than 4 V.[16] These results demonstrate that the uniform coating layer on the surface of the CNT can effectively prevent direct contact between the discharge product Li_2O_2 and the CNT, and thereby prevent or reduce the formation of the side product Li_2CO_3. Furthermore, the concept of the core–shell-structured bifunctional catalyst can be readily applied to other cathode systems for Li–O_2 batteries.

In summary, a RuO_2 shell uniformly coated on the surface of core CNTs by a simple sol–gel method, and the resulting composite was used as a catalyst in a rechargeable Li–O_2 battery. The CNT@RuO_2 composite demonstrated bifunctional catalytic activity for both the ORR and the OER in Li–O_2 batteries. The cell showed a high round-trip efficiency (ca. 79%) at a current of $100\ \mathrm{mA\,g_{total}^{-1}}$ and excellent electrochemical characteristics, such as high rate performance and good cycling performance. The capacity at a current of $500\ \mathrm{mA\,g_{total}^{-1}}$ reached $790\ \mathrm{mA\,h\,g^{-1}}$, which is about 70% of that at a current of $100\ \mathrm{mA\,g_{total}^{-1}}$. The discharge and charge potentials of the Li–O_2 battery showed almost no change over 20 cycles with a fixed capacity of $500\ \mathrm{mA\,h\,g^{-1}}$ at a current of $100\ \mathrm{mA\,g_{total}^{-1}}$. The specific capacity of the Li–O_2 cell was constant over 100 cycles at a high current of $500\ \mathrm{mA\,g_{total}^{-1}}$. This excellent performance can be ascribed to the ability of the RuO_2 coating layer on the CNTs to effectively prevent direct contact between the CNTs and the discharge product Li_2O_2 and thus to prevent or reduce the formation of Li_2CO_3, which can induce large polarization and may lead to charge failure. This kind of core–shell structure can be applied to other materials. The round-trip efficiency and the electrolyte are still challenges for the construction of rechargeable non-aqueous Li–O_2 batteries. Therefore, further studies should be focused on the development of highly effective bifunctional catalysts and stable electrolytes.

Received: September 11, 2013

Keywords: bifunctional catalysts · carbon nanotubes · core–shell structures · lithium–air batteries · ruthenium

[1] K. Abraham, Z. Jiang, *J. Electrochem. Soc.* **1996**, *143*, 1–5.

[2] a) T. Zhang, H. Zhou, *Angew. Chem.* **2012**, *124*, 11386–11403; *Angew. Chem. Int. Ed.* **2012**, *51*, 11224–11229; b) P. G. Bruce, S. A. Freunberger, L. J. Hardwick, J.-M. Tarascon, *Nat. Mater.* **2012**, *11*, 19–29; c) Y.-C. Lu, H. A. Gasteiger, Y. Shao-Horn, *J. Am. Chem. Soc.* **2011**, *133*, 19048–19051; d) J. J. Xu, D. Xu, Z. L. Wang, H. G. Wang, L. L. Zhang, X. B. Zhang, *Angew. Chem.* **2013**, *125*, 3979–3982; *Angew. Chem. Int. Ed.* **2013**, *52*, 3887–3890; e) S. A. Freunberger, Y. Chen, N. E. Drewett, L. J. Hardwick, F. Bardé, P. G. Bruce, *Angew. Chem.* **2011**, *123*, 8768–8772; *Angew. Chem. Int. Ed.* **2011**, *50*, 8609–8613; f) L. Suo, Y.-S. Hu, H. Li, M. Armand, L. Chen, *Nat. Commun.* **2013**, *4*, 1481; g) J.-J. Xu, Z.-L. Wang, D. Xu, L.-L. Zhang, X.-B. Zhang, *Nat. Commun.* **2013**, *4*, 2438.

[3] a) B. McCloskey, A. Speidel, R. Scheffler, D. Miller, V. Viswanathan, J. Hummelshøj, J. Nørskov, A. Luntz, *J. Phys. Chem. Lett.* **2012**, *3*, 997–1001; b) Y.-C. Lu, D. G. Kwabi, K. P. Yao, J. R. Harding, J. Zhou, L. Zuin, Y. Shao-Horn, *Energy Environ. Sci.* **2011**, *4*, 2999–3007.

[4] a) G. Girishkumar, B. McCloskey, A. Luntz, S. Swanson, W. Wilcke, *J. Phys. Chem. Lett.* **2010**, *1*, 2193–2203; b) J.-L. Shui, J. S. Okasinski, P. Kenesei, H. A. Dobbs, D. Zhao, J. D. Almer, D.-J. Liu, *Nat. Commun.* **2013**, *4*, 2255.

[5] a) Z. Guo, D. Zhou, X. Dong, Z. Qiu, Y. Wang, Y. Xia, *Adv. Mater.* **2013**, in press; b) R. R. Mitchell, B. M. Gallant, C. V. Thompson, Y. Shao-Horn, *Energy Environ. Sci.* **2011**, *4*, 2952–2958.

[6] A. Débart, J. Bao, G. Armstrong, P. G. Bruce, *J. Power Sources* **2007**, *174*, 1177–1182.

[7] a) F. Li, R. Ohnishi, Y. Yamada, J. Kubota, K. Domen, A. Yamada, H. Zhou, *Chem. Commun.* **2013**, *49*, 1175–1177; b) Y. Cao, Z. Wei, J. He, J. Zang, Q. Zhang, M. Zheng, Q. Dong, *Energy Environ. Sci.* **2012**, *5*, 9765–9768.

[8] B. M. Gallant, R. R. Mitchell, D. G. Kwabi, J. Zhou, L. Zuin, C. V. Thompson, Y. Shao-Horn, *J. Phys. Chem. C* **2012**, *116*, 20800–20805.

[9] F. Li, T. Zhang, H. Zhou, *Energy Environ. Sci.* **2013**, *6*, 1125–1141.

[10] Z. Peng, S. A. Freunberger, Y. Chen, P. G. Bruce, *Science* **2012**, *337*, 563–566.

[11] H.-G. Jung, Y. S. Jeong, J.-B. Park, Y.-K. Sun, B. Scrosati, Y. J. Lee, *ACS Nano* **2013**, *7*, 3532–3539.

[12] J. Zhou, H. Fang, Y. Hu, T. Sham, C. Wu, M. Liu, F. Li, *J. Phys. Chem. C* **2009**, *113*, 10747–10750.

[13] a) J. P. Paraknowitsch, J. Zhang, D. Su, A. Thomas, M. Antonietti, *Adv. Mater.* **2010**, *22*, 87–92; b) Z. Jian, L. Zhao, R. Wang, Y.-S. Hu, H. Li, W. Chen, L. Chen, *RSC Adv.* **2012**, *2*, 1751–1754.

[14] a) S. Mar, C. Chen, Y. Huang, K. Tiong, *Appl. Surf. Sci.* **1995**, *90*, 497–504; b) L.-j. Meng, V. Teixeira, M. P. dos Santos, *Thin Solid Films* **2003**, *442*, 93–97.

[15] F. Li, T. Zhang, Y. Yamada, A. Yamada, H. Zhou, *Adv. Energy Mater.* **2012**, *2*, 532–538.

[16] T. Zhang, H. Zhou, *Nat. Commun.* **2013**, *4*, 1817.